

# **Investigation of metal distribution and carbide crystallite formation in metal-doped carbon films (a-C:Me, Me=Ti, V, Zr, W) with low metal content**

Christoph Adelhelm<sup>1\*</sup>, Martin Balden<sup>1</sup>, Marcin Rasinski<sup>1,2</sup>, Stefan Lindig<sup>1</sup>, Thomas Plocinski<sup>2</sup>, Edmund Welter<sup>3</sup> and Marcin Sikora<sup>4,5</sup>

<sup>1</sup>Max-Planck-Institut für Plasmaphysik, Materials Research, EURATOM Association, Boltzmannstraße 2, 85748 Garching, Germany

<sup>2</sup>Faculty of Materials Science and Engineering, Warsaw University of Technology, ul. Wołoska 141, 02-507 Warsaw, Poland

<sup>3</sup>HASYLAB at Deutsches Elektronen-Synchrotron A Research Centre of the Helmholtz Association, Notkestr. 85, 22607 Hamburg, Germany

<sup>4</sup>European Synchrotron Radiation Facility, 6 rue Jules Horowitz, 38043 Grenoble, France

<sup>5</sup> Faculty of Physics and Applied Computer Science, AGH University of Science and Technology, Av. Mickiewicza 30, 30-059 Kraków, Poland

Dr. C. Adelhelm, [Christoph.adelhelm@ipp.mpg.de](mailto:Christoph.adelhelm@ipp.mpg.de) Phone: +49-170-1550981 Fax: M. Balden

Dr. M. Balden, [martin.balden@ipp.mpg.de](mailto:martin.balden@ipp.mpg.de) Phone: +49-89-3299-1688 / -1212 (Fax)

M. Rasinski, [mrasin@o2.pl](mailto:mrasin@o2.pl) Tel: +48-22-234-8109 / -8750 (Fax)

S. Lindig, [stefan.lindig@ipp.mpg.de](mailto:stefan.lindig@ipp.mpg.de) Phone: +49-89-3299-1262 / -1212 (Fax)

Dr. T. Plocinski, [tplocinski@inmat.pw.edu.pl](mailto:tplocinski@inmat.pw.edu.pl) Phone +48-22-234-8109 / -8750 (Fax)

Dr. E. Welter, [edmund.welter@desy.de](mailto:edmund.welter@desy.de), +49-40-8998-4510 / -2787 (Fax)

Dr. M. Sikora, [marcin.sikora@agh.edu.pl](mailto:marcin.sikora@agh.edu.pl) Phone: +48 12 6172304 / +48 12 6341247 (Fax)

---

\* Corresponding author: C. Adelhelm ([christoph.adelhelm@ipp.mpg.de](mailto:christoph.adelhelm@ipp.mpg.de))

## Abstract

Metal-doped amorphous carbon films (a-C:Me) were produced at RT by magnetron sputtering using a metal (Me=Ti, V, Zr, W) and graphite target. The metal distribution and the temperature-induced carbide crystallite formation was analyzed by X-ray diffraction (XRD), electron microscopy (TEM, STEM) and X-ray absorption spectroscopy (EXAFS, XANES), focusing on low metal concentrations between 6.5 and 9.5 %. In as-deposited samples, the metal atoms are atomically distributed in the carbon matrix without significant formation of carbide particles. With annealing to 900 K the local atomic environment around the metal atoms becomes similar to the carbide. The carbide crystallites grow with annealing up to 1300 K, their size is depended on the metal type:  $V > Ti > Zr \approx W$ .  $W_2C$  and  $WC_{1-x}$  crystallites were identified for W-doped films, whereas the monocarbides are formed for the other metals. It is demonstrated, that EXAFS and high resolution electron microscopy are required to get a correct picture of the structure of the analyzed a-C:W films.

## 1. Introduction

Metal-containing carbon films (a-C:Me, a-C:H:Me) were intensively studied in the last years and have great importance for application as hard and wear resistant coatings. Most frequently, the carbide forming metals Ti and W are used as dopants [1-7]. Improved tribological and mechanical properties compared to pure carbon films are achieved by a nanocomposite structure with nanometer-sized carbide particles in an amorphous matrix of (hydrogenated) carbon. Such coatings are also investigated in respect to improved optical and electrical properties [8, 9].

Our interest in a-C:Me films is motivated by research on the chemical sputtering process of carbon by hydrogen impact [10]. This is of great importance for future fusion devices like ITER, where carbon – together with Be and W – is suggested as plasma-facing material (PFM) [11]. The reaction of hydrogen species with carbon-based PFM leads to its degradation and to formation of undesired hydrocarbon layers, depositing in the reactor vessel [12]. If radioactive tritium is used – together with deuterium the fuel for fusion – this leads to an accumulating radioactive inventory, which is of high safety relevance. Doping of graphite with carbide-forming transition metals (Ti, V, Zr, W) is a possible way to decrease its reactivity against hydrogen species [10, 13, 14]. The presence of metals influence the erosion mechanism, and accumulate at the surface as a result of preferential sputtering of carbon [15, 16]. For a systematic investigation of the effect of doping, erosion experiments have been performed with metal-doped amorphous carbon films (a-C:Me), produced by dual source magnetron sputter deposition. Their reactivity against hydrogen is determined by the kind of metal and its concentration [17, 18], but depends also on the nano-structure of these layers [19]. To study particularly the effect of the a-C:Me nanostructure on the erosion process, the films were deposited at room temperature (RT) and annealed after deposition to induce structural changes.

Therefore, our deposition conditions are in contrast to most publications dealing with characterization of a-C:Me films optimized for tribological applications. For those, the formation of a stable carbide phase in the carbon matrix already during deposition is desired, which requires high adatom mobility. This can be achieved either by increased substrate temperature or by a high energy of the impinging species (e.g. by using ion-beams [20], CVD/PVD hybrid deposition [21, 22], plasmas with higher ionization [23, 24], laser ablation [25]). A higher metal content is also beneficial for carbide phase formation [9, 26]. Also a sample bias is generally applied to increase the energy deposited in the growing film during deposition.

In contrast, this paper gives a detailed structural analysis of a-C:Me (Me=Ti, V, Zr, W) films with low metal content (1-19%) and the films were deposited at RT by non-reactive magnetron sputtering without bias. We focus on samples with 6.5-9.5 % metal content and describe the metal distribution after film deposition and the temperature-induced carbide cluster formation by annealing up to 1300 K. The following methods were used: X-ray diffraction (XRD), (scanning) transmission electron microscopy (TEM, STEM), and X-ray absorption fine structure spectroscopy (XAFS) in the extended energy (EXAFS) and near edge (XANES) region. The influence on the carbon structure was studied by Raman spectroscopy and XRD, and the results have been published in a separate paper [27]. A catalytic effect on the  $sp^2$  clustering in the carbon phase during film deposition has been observed, which is dependent on the type of metal ( $W < V < Ti \approx Zr$ ).

## **2. Experimental**

### **2.1 a-C:Me film deposition and composition**

The a-C:Me films (Me = Ti, V, W, Zr) were deposited on Si (100) wafers by magnetron sputtering using a graphite and a metal cathode with argon as sputtering gas. The thickness

varied from about 0.7 to 1.5  $\mu\text{m}$ . Details of the film preparation can be found elsewhere [27, 28]. The atomic film composition was determined by Rutherford backscattering spectroscopy using a 3 MV tandem accelerator. All concentration values are given in at.%. After deposition the samples were annealed at 700, 900, 1100 and 1300 K in high vacuum for 15 minutes.

## **2.2 XRD**

The crystallographic phase and size of carbide crystallites formed in a-C:Me films were determined by XRD using a Seifert XRD 3003 PTS diffractometer operated with Cu  $K\alpha$  radiation. The experimental setup was optimized to measure thin films applying a parabolic multilayer mirror on the primary side to achieve a parallel beam and almost complete  $K\beta$  suppression. On the secondary side, a parallel plate collimator was installed to prevent detection of non-parallel beam intensity. Diffractograms were acquired as theta-scans at a fixed grazing incidence angle of  $1^\circ$ . For texture measurements the beam was restricted to 1  $\text{mm}^2$  at the primary side. Small samples ( $\approx 5 \times 5 \text{ mm}^2$ ) were mounted on Si wafers to exclude contributions from the sample holder. The Scherrer formula with a pre-factor of 1 was used for the estimation of the carbide crystallite size [29] under the assumption that peak broadening is dominated by the small crystallite size. An experimental line width of about  $0.3^\circ$  was determined for the Si (111) peak at  $2\theta = 28.4^\circ$  for the used setup. Nevertheless, since the observed peaks are generally much broader, its influence on the crystallite size determination was neglected. The peak FWHM was obtained by fitting PearsonVII profiles to the partly overlapping (100) and (111) diffraction peaks using the program fityk (0.7.6) [30], including a linear background. Error bars were derived from the uncertainty introduced by the fitting procedure.

## 2.3 Microscopy

For TEM analysis a set of samples of annealed a-C:V and a-C:Ti films on silicon wafers were prepared by ion polishing and analyzed with a Philips EM 430 operated at 300 kV. Estimation of the average carbide crystallite size was performed by analyzing about 200-400 particles, giving the average diameter with standard deviation. A focused ion beam microscope (FIB) was used for the preparation of a thin lamella of 6.5% and 9.5 % a-C:W samples. Argon ion milling in a Gentle Mill device was applied for final thinning and elimination of defects introduced by FIB. STEM observation was carried out on a 200 kV UHR STEM microscope (Hitachi HD-2700) equipped with a  $C_s$  corrector. Nano diffraction with the STEM was applied for single crystal phase analysis.

## 2.4 XAFS measurements

XAFS measurements at the *K* absorption edges of Ti, V and Zr as well as the W *L3*-edge were performed at HASYLAB (Hamburg) on beamline C. XAFS spectra of a-C:Me films were acquired in fluorescence yield mode using a 7 channel HPGe-detector (Canberra, Olen, Belgium) perpendicular to the incident X-ray. A Si (111) double crystal monochromator was used at the Ti and V edge, a Si (311) crystal was applied for Zr and W. All measurements were performed at room temperature.

For measurement of pure carbides (as powders,  $W_2C$  as sintered particle) total electron yield detection was applied. The measured energy range was about -200 eV to +800 eV in respect to the used absorption edge of the metal. The software ATHENA [31] was used for data analysis and extraction of the EXAFS data.

The W *L1*-edge measurements limited to the edge-near region (i.e. XANES) were performed at beamline ID26 of ESRF (Grenoble). A Si (311) double crystal monochromator was applied

134 to collect high resolution XANES spectra at the maximum of the W  $L_{\beta 3}$  emission line (9819  
135 eV), detected by a spectrometer consisting of a Si (660) analyzer crystal and an avalanche  
136 photodiode. The spectra were measured from 12080-12150 eV incident photon energy and  
137 normalized to the edge step at the highest energy.

### 3. Results

For this study, a-C:Me films (Me = Ti, V, Zr, and W) with metal concentrations from 1 up to 19 % were investigated by XRD, TEM/STEM and X-ray absorption techniques. The presented results are focused on carbon films with similar metal concentrations, ranging from 6.5 to 9.5 %. If different results are obtained for lower (1-3.5 %) or higher (up to 11-19 %) concentrations, it will be noted.

#### 3.1 XRD and electron microscopy

##### 3.1.1 Ti, V and Zr-doped films

The X-ray diffractograms for an annealing series of a 7.5% a-C:Ti film are shown in Fig. 1a. For the as-deposited and 700 K annealed samples no indication for TiC formation can be observed from the diffractograms. In a recent study by Lewin et al. [9] a 12 % Ti containing a-C:Ti film also remained X-ray amorphous. The weak bump around  $43^\circ$  is due to scattering from the carbon phase [27]. Annealing to 900 K and higher leads to occurrence of peaks which can be attributed to the (111) and (200) reflection of TiC. A similar picture was observed for a 8.5 % V containing film (Fig. 1b).

The diffraction patterns of the 7 % a-C:Zr film are depicted in Fig. 1c. A broad bump around  $31^\circ$  occurs already for the as-deposited sample. After annealing to 900 K a slight increase in intensity and a shift of the maximum to  $32^\circ$  can be observed. For 1100 K the diffraction pattern exhibits signals which can be attributed to the (111) peak with a shoulder referring to (200), and the (220) reflection of ZrC. For 1300 K, all three ZrC peaks are clearly developed.

The formed carbide particles are in the nanometer range as shown in Fig. 2 for a-C:V films, where the VC crystallite sizes are presented for 4 different metal concentrations, calculated by using the Scherrer formula. A clear carbide signature below 900 K was only visible for the



19% V containing film. Generally, the carbide particle size in a a-C:V film of a given concentration is increasing with the annealing temperature. After annealing to 1300 K the crystallite size is inversely proportional to the V concentration in the film. Evaluation of the crystallite size was also done by TEM for 3 specimens, confirming the size determined by XRD (Fig. 2). A TEM micrograph of the 1.5 % a-C:V sample annealed to 1300 K is presented in Fig. 3. It clearly shows that the carbide particles have a broad size distribution, which is reflected in the large standard deviation of the crystallite size determined by TEM (Fig. 2).

Fig. 4 summarizes carbide particle sizes derived from XRD for Ti, V, and Zr-doped films annealed from 900 up to 1300 K. From this graph the influence of the metal type on the particle size can be observed. For the 1300 K data, no overlap between the different dopants occurs, showing best the general trend in crystallite size:  $\text{ZrC} < \text{TiC} < \text{VC}$ . An explanation for this sequence can be given by comparing the carbide melting temperatures, which can be regarded as a measure for the carbide crystallite stability:  $\text{ZrC} (3693 \text{ K}) > \text{TiC} (3340 \text{ K}) > \text{VC} (3103 \text{ K})$  [32]. The lower the carbide crystal stability, the lower the temperature at which metal atoms can leave the surface of a carbide particle to diffuse to another particle, which gains in size (Ostwald ripening process).

### 3.1.2 a-C:W

Fig. 5 shows the evolution of the diffraction patterns of a 9.5% a-C:W film. Even without annealing an intensive, broad peak can be observed around  $37.4^\circ$ . With annealing, the peak maximum shifts slightly to higher angles ( $38.6^\circ$  for 1300 K), becomes more intensive and decreases in width. The FWHM reduces from  $11.3^\circ$  (as-deposited) to  $6.1^\circ$  (1300 K). Two other peaks can be separated at  $62^\circ$  and  $75^\circ$  for annealing to  $\geq 1100 \text{ K}$ .

Similar spectra were observed for a 6.5% a-C:W film; only the intensities in the diffractograms of the broad peaks are lower.

The broad diffraction peak around  $37^\circ$  is well known for C-W films and reported in earlier publications [8, 20, 22, 23, 25, 33]. It is generally explained by the formation of very small  $WC_{1-x}$  crystallites with preferred (111) orientation and high degree of disorder/amorphization. However, to our knowledge, no proof of the texture by pole figure analysis has been published. Also, unambiguous diffraction rings in TEM are often found for high energy deposition and/or higher W concentrations [6, 20, 22]. The maximum of the peak for the diffractogram after deposition fits to the (111) peak of  $WC_{1-x}$  at  $37^\circ$ , and the maximum for 1300 K coincides with the (002) reflection of  $W_2C$ . However, since a) no other peaks can be used to verify the phase and b) both peaks are not the most intensive for each carbide phase, no assignment of a tungsten carbide phase was done on the basis of our XRD data. Texture analysis on the nominal angles of diffraction peaks of WC,  $W_2C$  and  $WC_{1-x}$  confirm unambiguously that the missing appearance of further peaks due to strong texture can be excluded. An influence of changes in the film stress state during annealing on the observed shift of the peak at  $37^\circ$  can be excluded: The calculated stress would be in the order of 15 GPa which cannot not be accommodated in the film.

As described above, the unambiguous identification of a crystallographic phase in the a-C:W sample is not possible by XRD. Therefore, no evaluation by the Scherrer formula was performed, and no data for a-C:W is included in Fig. 4. By conventional TEM analysis, no crystalline carbide particles could be detected even in annealed a-C:W films (only diffuse dark spots were observed for 1300 K annealed samples). High resolution STEM analysis showed also no crystalline carbide particles in the as-deposited 9.5 % a-C:W sample. However, for the 1300 K annealed specimen, small carbide particles with a diameter of up to 3 nm could be observed (Fig. 6a). Fig. 6b shows the same area in the Z contrast mode. Here, regions enriched in W appear bright, carbon appears dark. It shows also W-rich regions with clusters sizes in the order of 1 nm.

Local nano diffraction of single particles revealed the presence of the  $W_2C$  as well as the  $WC_{1-x}$  phase. From 9 analyzed particles, 5 were labeled as  $WC_{1-x}$  and 4 as  $W_2C$ . A 1300 K annealed 6.5 % a-C:W sample showed also both phases and similar particle sizes.

## 3.2 XAFS

In contrast to XRD and TEM analysis, XAFS analysis does not require a crystalline phase. It is a local atomic probe, and only the atomic environment in a few Å distance around the metal atom contributes to the signal [34].

### 3.2.1 a-C:Ti and a-C:V

Fig. 7a shows XAFS spectra of the 7.5 % a-C:Ti sample, annealed up to 1300 K, as well as the spectrum of a TiC standard. The spectra of the as-deposited and 700 K annealed samples show only one broad bump after the edge. After annealing to 900 K the signal is more structured and for higher temperatures the spectra correspond to the spectrum of the TiC standard.

The XANES region is shown in Fig. 7b. The absorption edge shifts to higher energy with increasing annealing temperature; for the 1300 K annealed sample the edge position corresponds to that of the TiC standard. This trend is probably related to a better Ti-C bonding with increased electron transfer from Ti to C. The position of the first peak above the absorption edge does not vary, but slightly increases in intensity with annealing. The pre-edge region is magnified in the inset of Fig. 7b. It shows that the pre-edge part around 4968 eV decreases in intensity with annealing temperature, indicating a change in symmetry [35].

Fig. 8 shows the EXAFS data after Fourier transformation ( $k=2-8.5 \text{ Å}^{-1}$ ). In this representation, the EXAFS is plotted in radial distance to the Ti atom. The data is not

corrected for the phase shift, therefore the  $R$  gives no real atomic distances. A first neighbor peak is present around  $R=1.5$  Å. This first shell corresponds to carbon atoms, and no defined second shell from a Ti next neighbor (as in TiC) occurs. However, a shoulder at the higher  $R$  side can be observed which gains intensity for the 700 K sample. With annealing to 900 K, the second peak at 2.4 Å – corresponding to the second shell (Ti-Ti) – is well developed. For 900 K and higher temperatures, the local atomic environment of Ti is identical to TiC.

EXAFS data after Fourier transformation for as-deposited a-C:Ti films with different concentrations are shown in Fig. 9. For 1 % Ti, an intensive peak at lower  $R$  compared to the 7.5 % film occurs. For the 13 % a-C:Ti film, the Ti shell is visible. The intensive peak for 1% Ti could be attributed to the formation of a first shell consisting of O atoms (an oxygen concentration of about 2 % was determined by RBS). The Ti-O distance (1.93-1.96 Å) is shorter than the Ti-C distance (2.16 Å). In addition, the Ti edge energy position of the 1 % a-C:Ti film is higher than for all other as-deposited a-C:Ti films (e.g. 1.2 eV higher as for the 7.5 % Ti doped film). This can be explained by the more polar Ti-O bond and a more pronounced electron transfer from Ti to O compared to C. Annealing of the 1 % a-C:Ti sample up to 1100 K leads to an increasing intensity of the oxygen peak, but not to formation of TiO<sub>2</sub> crystallites. After annealing to 1300 K, the local environment changed and became similar to TiC. This sample showed no TiC diffraction peaks in XRD.

In general, the 8.5 % a-C:V EXAFS data shows a similar development for the annealing series, as obvious from Fig. 10a. No indication for an oxygen first shell can be observed for the as-deposited sample of 1.5 % V (Fig. 10b). The 19 % a-C:V film shows a VC-like local environment already after deposition which is confirmed by carbide peaks in XRD.

### 3.2.2 a-C:Zr and a-C:W

The as-deposited carbon films with 7 % Zr and especially the 9.5 % W show broad peaks in the X-ray diffractograms (Fig. 1c, Fig. 5). However, the EXAFS measurements show that carbide crystallites are only present in annealed samples: Fig. 11a presents EXAFS data for the Zr-doped sample after deposition and annealing to 900 and 1100 K. Only after annealing to 1100 K, the signal becomes similar to the ZrC standard. However, the signal intensity of the a-C:Zr film is lower, which is probably due to the small particle size and the use of electron yield detection for the ZrC standard. To show the influence of the second neighbor of Zr on the EXAFS signal, Fig. 11b gives  $|\chi(k)|$  of the as-deposited sample and the backtransformed data for  $R = 1.1-2.1 \text{ \AA}$  (data range of the first shell) and  $R = 1.1-3.5 \text{ \AA}$  (data range of the first and second shell).  $|\chi(k)|$  is mainly determined by scattering at the first neighbor; however, including the second shell ( $R=1.1-3.35 \text{ \AA}$ ) slightly improves the description of  $|\chi(k)|$  between  $k=6-8.5 \text{ \AA}^{-1}$ .

In Fig. 12a EXAFS data is presented for the 9.5% a-C:W sample and a  $W_2C$  standard. Only a first neighbor peak is observed for the as-deposited sample. Annealing up to 900 K only slightly changes  $|\chi(R)|$ . For the 1300 K annealed sample the signal becomes similar to the  $W_2C$  standard for the first and second shell ( $R = 1-3.5 \text{ \AA}$ ). However, the intensity is not fully reproduced and diminishes for  $R > 4 \text{ \AA}$ . Since STEM analysis showed the presence of  $W_2C$  and  $WC_{1-x}$  phase it is clear, that the EXAFS (which is an average over all W atoms) does not fully correspond to the  $W_2C$  standard spectrum. As obvious from Fig. 12b, no significant contribution of a second shell contributes to  $|\chi(k)|$  for the as-deposited sample.

EXAFS spectra for 14.5 % gave comparable results. For the 2.5 and 4 % W containing films, the second shell is not well developed even after annealing at 1300 K.

The XANES region of the spectra acquired at the W  $L_3$  edge is not very sensitive to the local electronic structure: the edge region is dominated by a strong white line due to transitions into almost empty 5d levels. In addition to EXAFS measurements, XANES measurements of a-

285 C:W films at the W  $L_1$  edge were performed to compare the local electronic environment of  
286 W in W-doped films with different W standard materials. Fig. 13 compares XANES spectra  
287 of W,  $W_2C$ , WC and  $WC_{1-x}$  [33, 36] with the spectra of a 6.5% a-C:W film (as-dep., 900 K,  
288 1300 K). It reveals significant difference of the shape and energy position of the reference  
289 spectra, which are the fingerprints of the local symmetry, coordination, and valence of the  
290 probed atom species [35]. The  $W_2C$ ,  $WC_{1-x}$  and WC spectra show a gradual shape evolution.  
291 Upon increasing W/C ratio the edge energy shifts towards lower energy.

292 The spectra of as-deposited and annealed samples are not identical, showing a clear difference  
293 especially in the pre-edge intensity. A gradual decrease of the pre-edge peak intensity with  
294 increasing the annealing temperature is observed, which is attributed to the enhancement of  
295 the average local symmetry around the W atoms upon annealing [37]. The spectrum of the  
296 1300 K annealed 6.5% a-C:W film is more similar to that of the  $W_2C$  reference than to that of  
297  $WC_{1-x}$ .

## 4. Discussion

The absence of a second shell (metal-metal) peak in the EXAFS data clearly shows that the metal atoms are distributed atomically disperse in the carbon matrix in as-deposited samples, surrounded by a carbon first shell. No significant carbide particle formation has occurred (except 19 % V). This finding is independent from the metal type. For 1 % Ti, a Ti-O first shell was proposed (Fig. 9). The results are related to the low metal content and especially the soft deposition conditions used in our preparation process (RT, no bias). Other publications dealing with the structural investigation of a-C:Me films report the formation of carbide crystallites even for lower [20, 21] or similar concentrations [38]. This can be attributed to the higher energies of the impinging species in these depositions (unbalanced magnetron, ion beam deposition). Also, significantly higher metal concentrations are used in most studies.

With annealing, carbide particle formation occurred in all samples, which is evident from the EXAFS data, but also from XRD. After annealing to 1300 K, the largest crystallites were observed for V-doping, the smallest particles were observed in Zr (Fig. 4) and W-doped films (Fig. 6). The relatively low melting point of the tungsten carbides (below 3100 K [39]) does not fit to the above mentioned inverse relation between melting point and carbide crystallite size for VC, Ti, ZrC. A possible explanation is, that the particle growth is not only limited by the binding energy of the metal atoms in a carbide crystallite, but also by the diffusion in the carbon matrix, which is the lowest for W due to its high atomic mass.

The X-ray diffractograms of as-deposited samples containing Zr and W (Fig. 1c and 5) show broad peaks, especially for W. As mentioned above, similar spectra are often found for C films containing W [8, 20, 22, 23, 25, 33] and are generally interpreted in a way that textured  $WC_{1-x}$  nanoparticles have been formed. However, our EXAFS analysis reveals that this interpretation does not correctly describe the structural situation in our a-C:W films: The majority of the W atoms is dispersed in the carbon matrix and not present in a carbide

particle. In addition, high resolution STEM analysis showed carbide particles only after annealing. For 1300 K, both  $W_2C$  and  $WC_{1-x}$  crystallites are present. This is also not reflected in the XRD pattern in Fig. 5. Still, only a single peak is present between  $2\theta = 30-50^\circ$ . Therefore, the X-ray diffractogram of the 1300 K annealed sample is at least a result of different crystallographic phases and small crystallite size. The texture analysis showed that the tungsten carbide particles have no preferred orientation. Therefore, a possible texture of the crystallites is not responsible for the missing peaks compared to the pure carbides. In addition, scattering from a small amount of W-C clusters below 1 nm with possible high distortion could contribute to the diffraction pattern. This would also be an explanation for the spectrum of the as-deposited a-C:W film. However, only a minor fraction of W atoms can be located in such clusters, because from the EXAFS results significant clustering of W atoms can be excluded. The combination of XRD, STEM and EXAFS analysis shows that the occurrence of the broad XRD peak around  $37^\circ$  does not always correspond to a carbon film containing  $WC_{1-x}$  crystallites.

For 3d transition metals, large pre-edge peaks in the XANES spectra are observed in low symmetry coordination while their intensity almost diminishes in structures characterized by inversion symmetry [35]. Therefore, the pre-edge intensity can be considered as an indication of local distortion. In the XANES spectra of the as-deposited 7.5 % a-C:Ti (Fig. 7b), a lower coordination number and high distortion around the Ti atom could explain the higher pre-edge peak intensity compared to TiC. With annealing, a higher symmetry is achieved due to increasing order and the formation and growth of TiC crystallites. This is also reflected in the shift of the edge position to higher energies, due to increased electron transfer from Ti to C. For the 6.5 % a-C:W sample, the W  $L_1$  XANES pre-edge also shows a decrease in intensity with annealing. On the other hand, no significant shift in the edge position is observed. The XANES of the 1300 K annealed sample is more similar to the  $W_2C$  standard than  $WC_{1-x}$ . However, STEM analysis clearly showed the occurrence of both phases. A XANES spectrum



is a result of all probed atoms and strongly depends on distortion, crystallographic phase and crystallite size. Therefore, XANES analysis could not be applied for phase determination in the investigated a-C:W films.

## 5. Summary

In as-deposited a-C:Me films (Me=Ti, V, Zr) with low metal concentrations no carbide particles could be observed after deposition, and the metal atoms are distributed atomically disperse in the carbon matrix under the here applied deposition conditions. The local atomic environment around the metal atoms was probed by EXAFS and becomes similar to the pure carbides after annealing to 900 K (Ti and V) or 1100 K (Zr). Samples annealed to 900 K and higher showed also carbide peaks in XRD. The carbide particle size depends on the metal species: V>Ti>Zr.

For W-doped films, broad peaks can be observed in the X-ray diffractograms already after deposition. However, EXAFS clearly shows that no significant carbide clustering is present in the samples. STEM analysis revealed up to 3 nm large  $WC_{1-x}$  and  $W_2C$  particles in samples annealed to 1300 K. This information cannot be deduced from the XRD data, and shows that relying only on XRD can lead to wrong conclusions for a-C:W films.

## Acknowledgement

The research leading to these results has received funding from the European Atomic Energy Community's Seventh Framework Program (FP7 / 2007-2011) under Grant Agreement No 224752. We acknowledge ESRF and HASYLAB for the provision of beam time and the ID26 staff for help in setting up the experiment.

## References

1. Voevodin, A.A., S.V. Prasad, and J.S. Zabinski, *Nanocrystalline carbide amorphous carbon composites*. Journal Of Applied Physics, 1997. **82**(2): p. 855-858.
2. Meng, W.J. and B.A. Gillispie, *Mechanical properties of Ti-containing and W-containing diamond-like carbon coatings*. Journal of Applied Physics, 1998. **84**(8): p. 4314-4321.
3. Stüber, M., et al., *Microstructure and properties of low friction TiC-C nanocomposite coatings deposited by magnetron sputtering*. Surface & Coatings Technology, 2002. **150**(2-3): p. 218-226.
4. Nilsson, D., et al., *Low-friction carbon-rich carbide coatings deposited by co-sputtering*. Wear, 2003. **254**(11): p. 1084-1091.
5. Pei, Y.T., D. Galvan, and J.T.M. De Hosson, *Nanostructure and properties of TiC/a-C : H composite coatings*. Acta Materialia, 2005. **53**(17): p. 4505-4521.
6. Abad, M.D., et al., *Tailored synthesis of nanostructured WC/a-C coatings by dual magnetron sputtering*. Surface & Coatings Technology, 2010. **204**(21-22): p. 3490-3500.
7. Sanchez-Lopez, J.C., et al., *Metal carbide/amorphous C-based nanocomposite coatings for tribological applications*. Surface & Coatings Technology, 2009. **204**(6-7): p. 947-954.
8. Abad, M.D., et al., *WC/a-C nanocomposite thin films: Optical and electrical properties*. Journal of Applied Physics, 2009. **105**(3): p. 033510.
9. Lewin, E., O. Wilhelmsson, and U. Jansson, *Nanocomposite nc-TiC/a-C thin films for electrical contact applications*. Journal of Applied Physics, 2006. **100**(5): p. 054303-10.

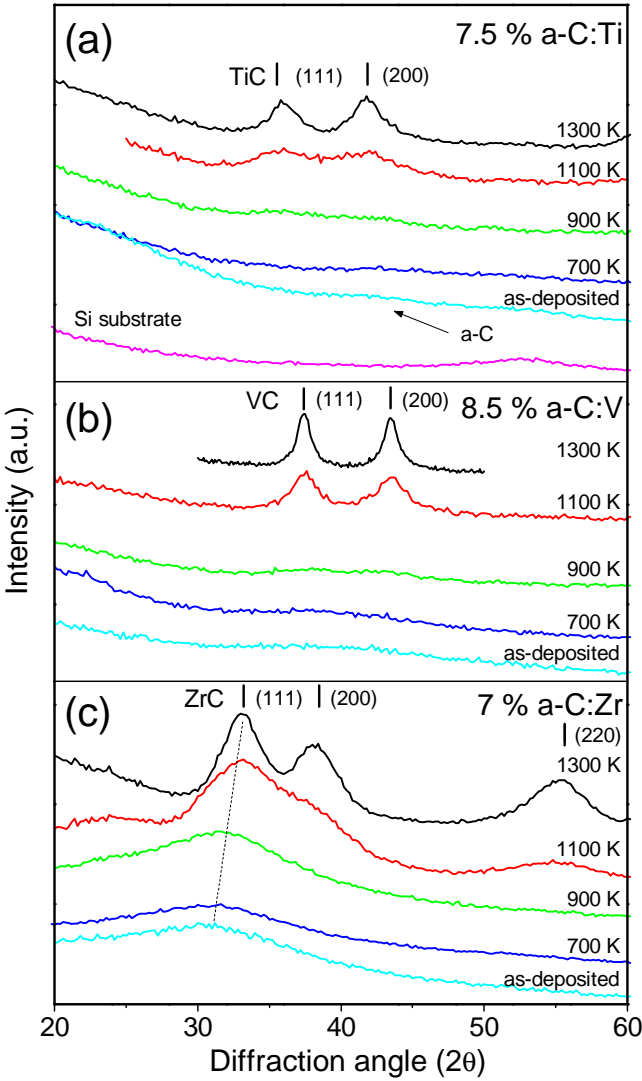
- 397 10. Jacob, W. and J. Roth, *Chemical Sputtering in Sputtering by Particle Bombardment.*  
398 *Experiments and Computer Calculations from Threshold to MeV Energies*, R.  
399 Behrisch and W. Eckstein, Editors. 2007, Springer: Berlin.
- 400 11. Barabash, V., et al., *Materials challenges for ITER - Current status and future*  
401 *activities*. Journal of Nuclear Materials, 2007. **367-370**(Part 1): p. 21-32.
- 402 12. Roth, J., et al., *Recent analysis of key plasma wall interactions issues for ITER.*  
403 Journal of Nuclear Materials, 2009. **390-91**: p. 1-9.
- 404 13. Balden, M., et al., *Chemical erosion of carbon doped with different fine-grain*  
405 *carbides*. Journal Of Nuclear Materials, 2001. **290**: p. 52-56.
- 406 14. Pardo, E.d.J., et al., *Erosion Processes of Carbon Materials under Hydrogen*  
407 *Bombardement and their Mitigation by Doping*. Physica Scripta, 2004. **T111**: p. 62-  
408 67.
- 409 15. Balden, M., *Overview on the effects of dopants on chemical erosion and RES of*  
410 *carbon-based materials*. Physica Scripta, 1999. **T81**: p. 64-69.
- 411 16. Salonen, E., et al., *Reduced chemical sputtering of carbon by silicon doping*. Journal  
412 of Applied Physics, 2002. **92**(4): p. 2216-2218.
- 413 17. Balden, M., et al., *Deuterium-induced chemical erosion of carbon-metal layers.*  
414 Journal of Nuclear Materials, 2005. **337-39**(1-3): p. 980-984.
- 415 18. Balden, M. and C. Adelhelm, *Characterization and erosion of metal-containing*  
416 *carbon films*. Physica Scripta, 2007. **T128**: p. 121-126.
- 417 19. Starke, P., C. Adelhelm, and M. Balden, *Erosion behaviour of metal-doped carbon*  
418 *layers in deuterium low pressure plasmas and the determination by optical emission*  
419 *spectroscopy*. Contributions to Plasma Physics, 2007. **47**(7): p. 530-536.
- 420 20. Wang, A.Y., et al., *Structure and mechanical properties of W incorporated diamond-*  
421 *like carbon films prepared by a hybrid ion beam deposition technique*. Carbon, 2006.  
422 **44**(9): p. 1826-1832.

- 423 21. Meng, W.J., R.C. Tittsworth, and L.E. Rehn, *Mechanical properties and*  
424 *microstructure of TiC/amorphous hydrocarbon nanocomposite coatings*. Thin Solid  
425 Films, 2000. **377**: p. 222-232.
- 426 22. Park, S.J., et al., *Microstructure and mechanical properties of WC-C nanocomposite*  
427 *films*. Diamond and Related Materials, 2002. **11**(10): p. 1747-1752.
- 428 23. Kao, W.H., *Optimized a-C : W-x% coatings with enhanced tribological properties and*  
429 *improved micro-drilling performance*. Surface & Coatings Technology, 2007. **201**(16-  
430 17): p. 7392-7400.
- 431 24. Pei, Y.T., et al., *Microstructural control of TiC/a-C nanocomposite coatings with*  
432 *pulsed magnetron sputtering*. Acta Materialia, 2008. **56**(4): p. 696-709.
- 433 25. Voevodin, A.A., et al., *Nanocrystalline WC and WC/a-C composite coatings produced*  
434 *from intersected plasma fluxes at low deposition temperatures*. Journal of Vacuum  
435 Science & Technology A, 1999. **17**(3): p. 986-992.
- 436 26. Meng, W.J., et al., *Ti atomic bonding environment in Ti-containing hydrocarbon*  
437 *coatings*. Journal of Applied Physics, 2000. **88**(5): p. 2415-2422.
- 438 27. Adelhelm, C., et al., *Influence of doping (Ti, V, Zr, W) and annealing on the sp<sup>[sup 2]</sup>*  
439 *carbon structure of amorphous carbon films*. Journal of Applied Physics, 2009.  
440 **105**(3): p. 033522-9.
- 441 28. Balden, M., et al., *Metal-doped carbon films obtained by magnetron sputtering*.  
442 Surface and Coatings Technology, 2005. **200**(1-4): p. 413-417.
- 443 29. Birkholz, M., *Thin Film Analysis by X-Ray Scattering*. 2006, Weinheim: Wiley-VCH
- 444 30. <http://www.unipress.waw.pl/fityk/>.
- 445 31. Ravel, B. and M. Newville, *ATHENA, ARTEMIS, HEPHAESTUS: data analysis for X-*  
446 *ray absorption spectroscopy using IFEFFIT*. Journal of Synchrotron Radiation, 2005.  
447 **12**: p. 537-541.
- 448 32. Pierson, H.O., *Handbook of Refractory Carbides and Nitrides*

- Properties, Characteristics, Processing and Applications*. Materials Science and Process Technology Series. 1996, Westwood: Noyes. 340.
33. Schiffmann, K.I., et al., *Sizes and distances of metal clusters in Au-, Pt-, W- and Fe-containing diamond-like carbon hard coatings: a comparative study by small angle X-ray scattering, wide angle X-ray diffraction, transmission electron microscopy and scanning tunnelling microscopy*. Thin Solid Films, 1999. **347**(1-2): p. 60-71.
34. Koningsberger, D.C. and R. Prins, *X-Ray Absorption. Principles, Applications, Techniques of EXAFS, SEXAFS and XANES*. Chemical Analysis, ed. W. J.D. Vol. 92. 1988, New York: John Wiley & Sons.
35. Yamamoto, T., *Assignment of pre-edge peaks in K-edge x-ray absorption spectra of 3d transition metal compounds: electric dipole or quadrupole?* X-Ray Spectrometry, 2008. **37**(6): p. 572-584.
36. The WC1-x thin film sample was received by K. Schiffmann, Fraunhofer Institut für Schicht- und Oberflächentechnik, Braunschweig, Germany. XRD data of this sample (55 % W) is published in [33].
37. Yamazoe, S., et al., *XAFS study of tungsten L-1- and L-3-edges: Structural analysis of WO<sub>3</sub> species loaded on TiO<sub>2</sub> as a catalyst for photo-oxidation of NH<sub>3</sub>*. Journal of Physical Chemistry C, 2008. **112**(17): p. 6869-6879.
38. Feng, B., et al., *Characterization of microstructure and mechanical behavior of sputter deposited Ti-containing amorphous carbon coatings*. Surface & Coatings Technology, 2001. **148**(2-3): p. 153-162.
39. Kurlov, A. and A. Gusev, *Tungsten carbides and W-C phase diagram*. Inorganic Materials, 2006. **42**(2): p. 121-127.

474  
475

Fig. 1



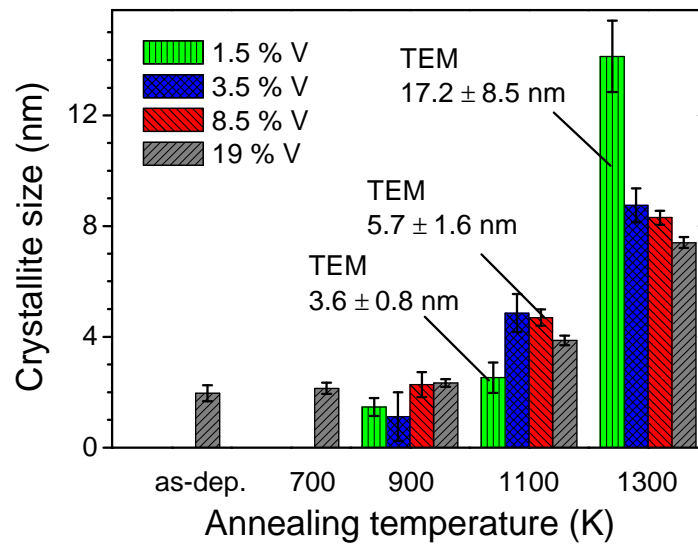
476

477

Fig. 2

478

479



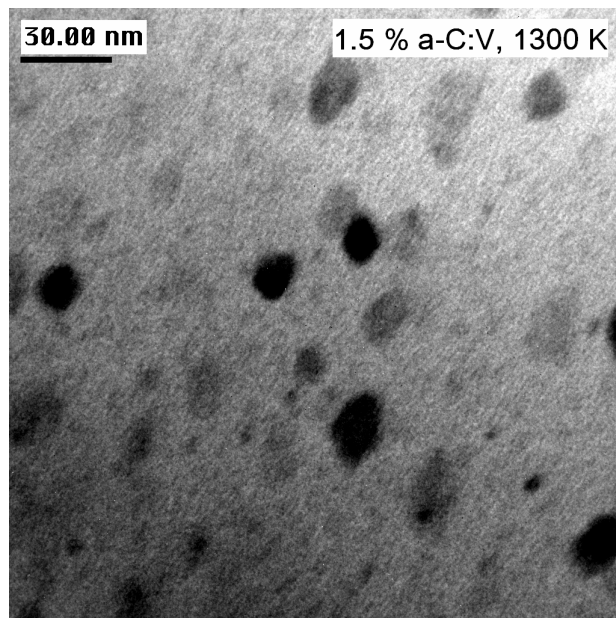
480

481

Fig. 3

482

483



484



Fig.. 4

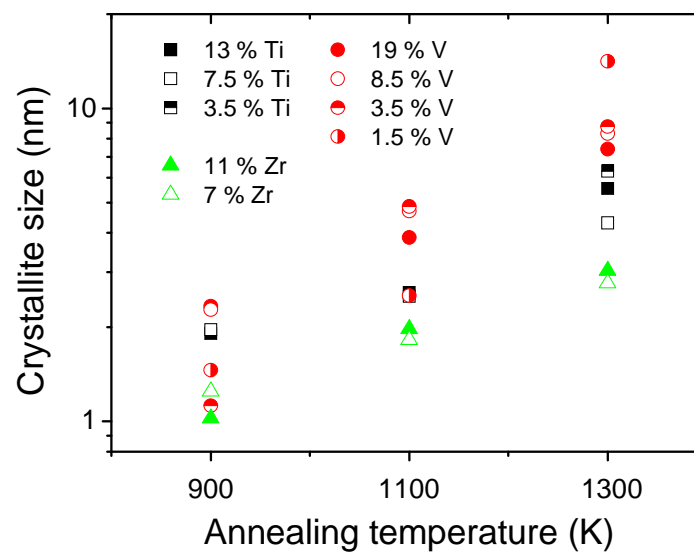
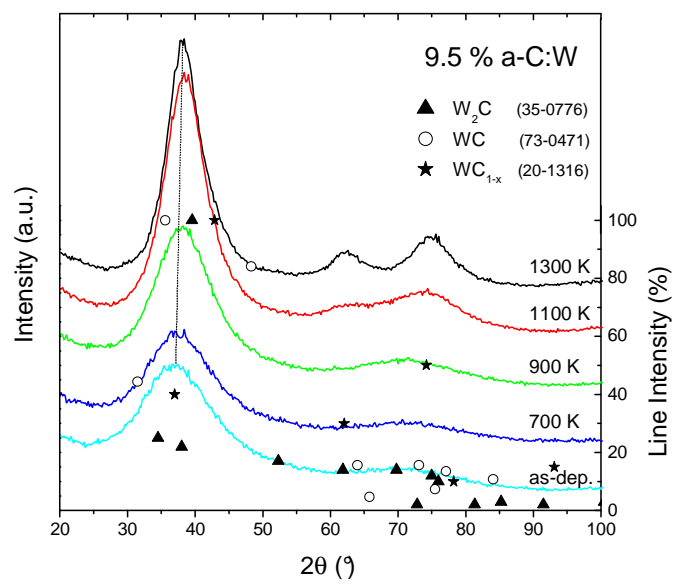
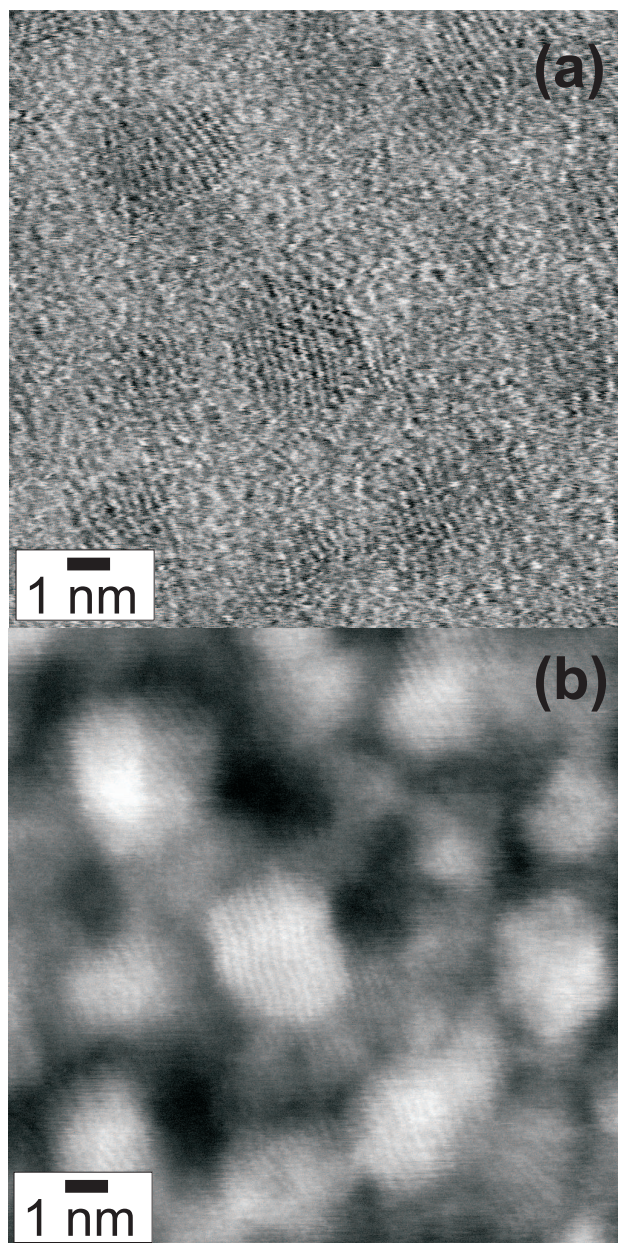


Fig. 5



493  
494  
495

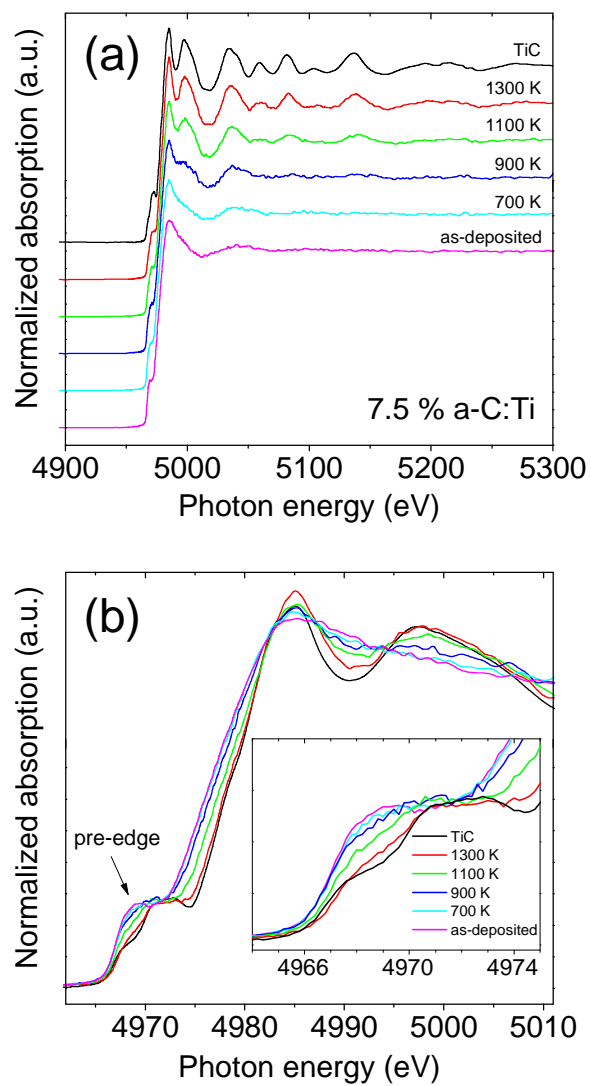
Fig. 6



496  
497

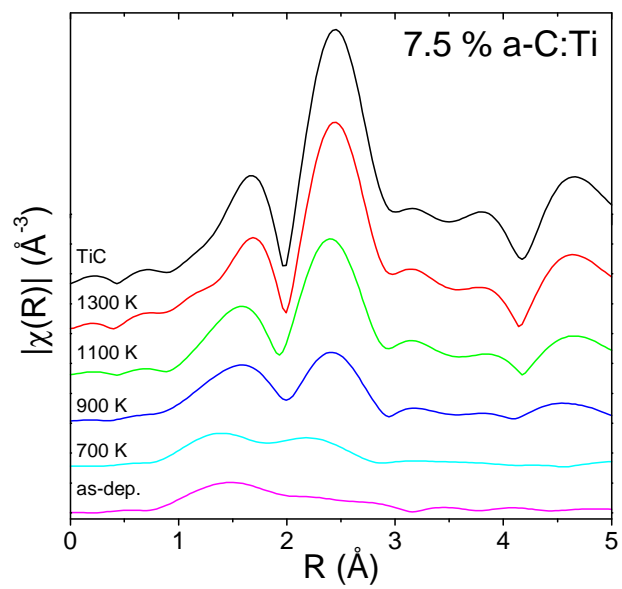
498  
499  
500

Fig. 7



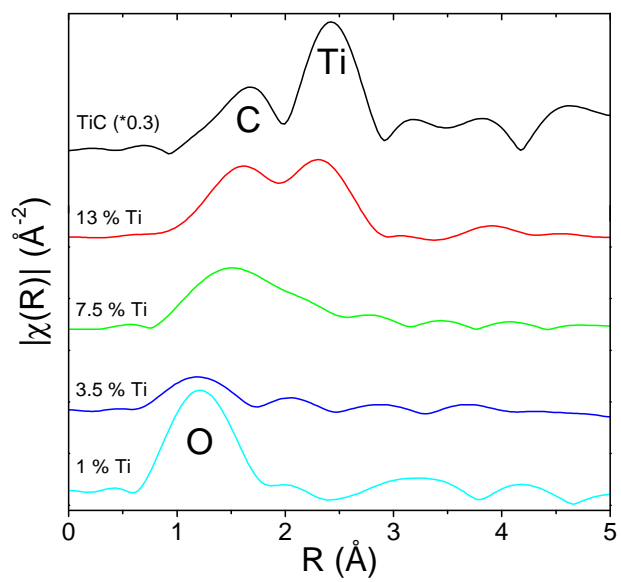
501

Fig. 8



507  
508  
509

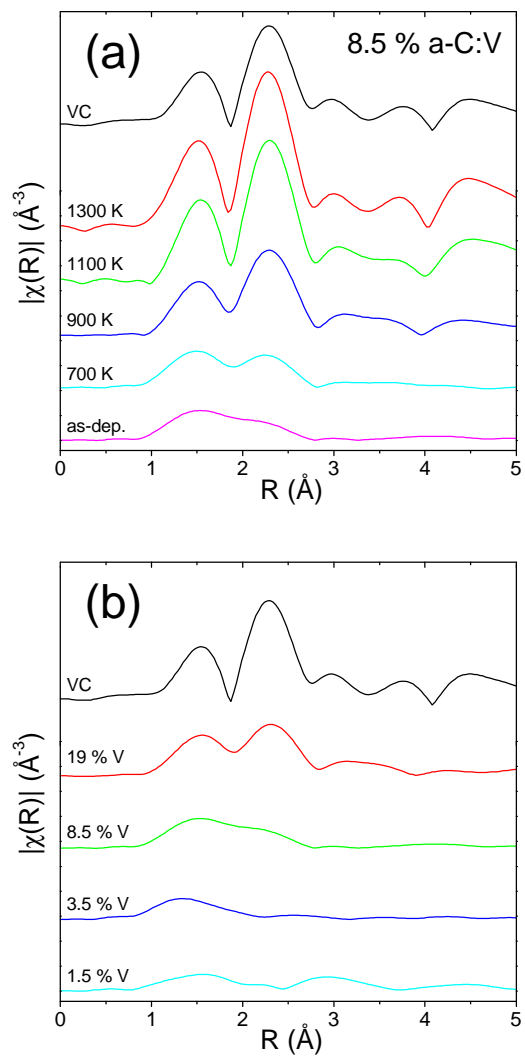
Fig. 9



510

511  
512  
513

Fig. 10



514

Fig. 11

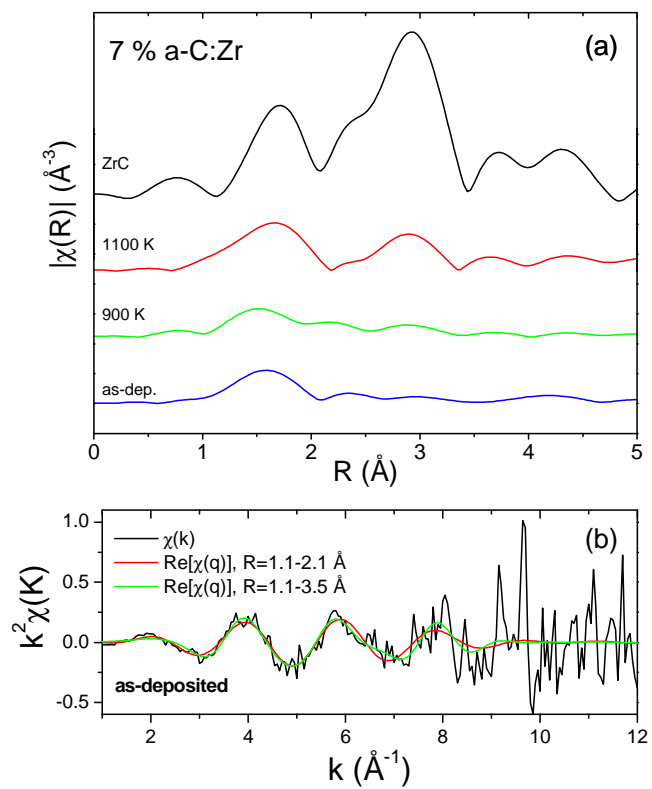
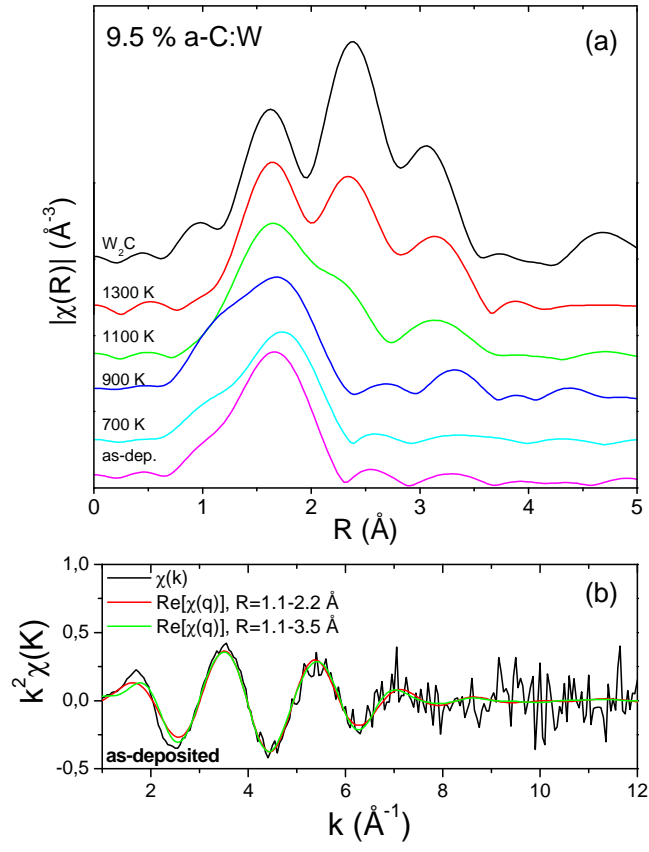


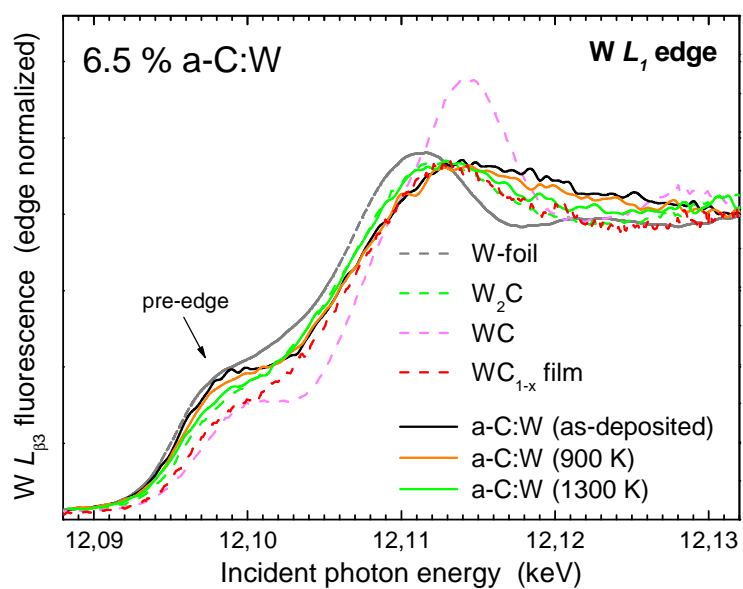


Fig. 12



525  
526  
527

Fig. 13



528

## List of Figure Captions

Fig. 1: X-ray diffractograms of a) 7.5 % a-C:Ti, b) 8.5 % a-C:V, c) 7 % a-C:Zr films after deposition and annealing up to 1300 K. Diffraction peaks for TiC, VC, and ZrC are indicated.

Fig. 2: Crystallite sizes for VC crystallites determined by XRD for a-C:V films with different concentrations and annealing temperatures up to 1300 K. Crystallite sizes determined by TEM are given for three samples. The errors represent the uncertainty introduced by the peak fitting procedure (XRD) or the particle size distribution (TEM).

Fig. 3: TEM micrograph of a 1.5 % V containing a-C:V film after annealing to 1300 K.

Fig. 4: Carbide crystallite sizes in Ti, V, and Zr-doped carbon films with different metal concentrations annealed to 900, 1100 and 1300 K. Note the logarithmic y-scale.

Fig. 5: X-ray diffractograms of 9.5 % a-C:W films after deposition and annealed up to 1300 K. Diffraction peaks for the carbide phases  $W_2C$ , WC and  $WC_{1-x}$  are shown, the used PDF card numbers of the ICDD database are indicated.

Fig. 6: a) STEM bright field micrograph of a 9.5 % a-C:W sample, annealed up to 1300 K. Electron diffraction of single particles revealed  $WC_{1-x}$  and  $W_2C$  phase. b) STEM Z contrast micrograph of the same area as in a).

Fig. 7: a) Normalized Ti K-edge XAFS spectra of 7.5 % a-C:Ti films annealed up to 1300 K and TiC standard. b) XANES region of the spectra in a). The inset shows the magnified region of the pre-edge peak

Fig. 8: EXAFS data of the annealing series of the 7.5 % a-C:Ti sample, after Fourier transformation of  $k^2\chi(k)$ ,  $k=2-8.5 \text{ \AA}^{-1}$ , not phase shift corrected.

Fig. 9: EXAFS data of as-deposited a-C:Ti films with different Ti concentrations and the TiC standard, after Fourier transformation of  $k\chi(k)$ ,  $k=2-8.5 \text{ \AA}^{-1}$ , not phase shift corrected.

Fig. 10: a) EXAFS data of the annealing series of the 8.5 % a-C:V sample, after Fourier transformation of  $k^2\chi(k)$ ,  $k=2-8.5 \text{ \AA}^{-1}$ , not phase shift corrected. b) EXAFS data of as-deposited a-C:V films with different V concentrations and the VC standard, after Fourier transformation of  $k^2\chi(k)$ ,  $k=2-8.5 \text{ \AA}^{-1}$ , not phase shift corrected.

Fig. 11 a) EXAFS data of the 7 % a-C:Zr sample after deposition and annealing to 900 and 1100 K, and a ZrC standard (after Fourier transformation of  $k^2\chi(k)$ ,  $k=2.5-8.5 \text{ \AA}^{-1}$ , not phase shift corrected). b)  $\chi(k)$  of the as-deposited sample and backtransformed data for  $R = 1.1-2.1 \text{ \AA}$  (data range of the first shell) and  $R = 1.1-3.5 \text{ \AA}$  (data range of the first and second shell).

Fig. 12 a) EXAFS data of the 9.5 % a-C:W sample after deposition and annealed up to 1300 K, and a  $W_2C$  standard (after Fourier transformation of  $k^2\chi(k)$ ,  $k=2-8.5 \text{ \AA}^{-1}$ , not phase shift corrected). b)  $k^2\chi(k)$  for the as-deposited sample and backtransformed data for  $R=1.1-2.2 \text{ \AA}$  (data range of the first shell) and  $R= 1.1-3.5 \text{ \AA}$  (data range of the first and second shell).

577

578 Fig. 13: Normalized W L<sub>1</sub> edge NEXAFS spectra of as-deposited and annealed (900 K, 1300  
579 K) 6.5 % a-C:W films and W standard materials.

580

581